

# Supersonic Cloud Collision - I

S. V. Anathpindika<sup>1\*</sup>

<sup>1</sup>*School Of Astronomy and Physics, Cardiff University, 5-The Parade, CF24 3AA*

Accepted 0000 March 00. Received 0000 March 00; in original form 0000 March 00

## ABSTRACT

Depending on the precollision velocity, colliding molecular clouds produce a slab that is either shock compressed or pressure confined. In a sequel of two papers (I & II), we investigate the evolution of such slabs. In the present paper (I) we study the effect of strong shear between slab layers on the dynamic evolution of a shock compressed gas slab. We find that a small perturbation on the surface of this slab is rapidly magnified through the non-linear growth of the shearing instability. Our simulations show evidence of the non-linear thin shell instability (NTSI) in the shock compressed slab. The NTSI causes rapid turbulent mixing between slab layers and leads to dissipation of thermal energy. Eventually the slab collapses to form a thin, long filament. Star formation commences in this filament. We examine both, head-on and off-centre cloud collisions in this paper.

**Key words:** Molecular clouds (MCs) – shock compressed gas slabs & filaments – NTSI – SPH.

## 1 INTRODUCTION

*Density structure and examples of nearby filamentary regions* : Spiral shock waves sweep up matter in galactic arms and produce large scale structure and dust lanes (Roberts 1969; Fleck 1992; Heitsch *et al* 2006; Elmegreen 2007). Often MCs themselves are filamentary and such clouds, presumably form out of gravitationally unstable gas sheets (Nagai, Inutsuka & Miyama 1998). Detailed studies of molecular line profiles of MCs have revealed that matter within them is highly unevenly distributed and gives them a clumpy appearance, which has led some workers to suggest a fractal model of MCs (Elmegreen 1997).

Schneider & Elmegreen (1979) performed one of the first studies of large scale filamentary structures in the local neighbourhood. Now with improved technology it is possible to map MCs in greater detail. For instance, dense filamentary structures have been observed in the Perseus region where there is evidence for ongoing star formation (Hatchell *et al* 2005). The Orion Integral Filament (OIF) in the Orion A region has been studied in great detail and a number of Young Stellar Objects (YSOs) have been reported to be embedded in it (Chini *et al.* 1997; Johnstone & Bally 1999).

*Structure formation mechanisms - briefly* : Structure within MCs appears to be hierarchical and the densest regions are gravitationally bound, see for instance Larson (1981) and Elmegreen (2007). Turbulence within MCs de-

cays rather quickly, on a timescale equal to the dynamical period of evolution of the cloud. It leads to dynamic interaction between fluid flows. This is one possible mechanism for structure formation in MCs (Klessen & Burkert 2000; McLow & Klessen 2004). Gas slabs resulting from collision of stellar winds from binary systems expanding at supersonic speeds become thermally unstable due to rapid cooling, also turbulent motion within shells makes them unstable to shearing instabilities (Stevens *et al* 1992). Similarly, powerful ionising radiation emitted by young OB associations or supernova remnants sweeps up gas and forms a dense shell that is gravitationally and thermally unstable (Strickland & Blondin 1995; Dale, Clark & Bonnell 2007). MC collision produces gravitationally unstable gas slabs (Bhattachal *et al* 1998).

The gas bodies resulting from dynamically interacting fluid masses already contain the necessary seeds of dynamic instability. Analogous to random motion of clumps within clouds, MCs in galactic arms are also in random motion. CO spectra of MCs suggest a non - Maxwellian velocity (orbital velocity of clouds) distribution in the range  $-100 \text{ km s}^{-1}$  to  $200 \text{ km s}^{-1}$  (Spitzer 1968; Solomon *et al* 1987). The velocity dispersion of random cloud motion is typically an order of magnitude smaller than this velocity. Supersonic cloud collision is generally inelastic and leads to kinetic energy dissipation.

A single cloud collision is expected to occur every few million years, which is why it is significant on the dynamic timescales of MCs. It is a violent phenomenon which might spawn star formation in the resulting compos-

\* E-mail:Sumedh.Anathpindika@astro.cf.ac.uk(SVA)

ite object. Magnetic fields threading galactic arms modulate cloud velocities, in which case cloud collisions are less energetic. Stronger magnetic fields along galactic arms cause greater modulation and therefore, even weaker cloud collisions (Spitzer 1968).

*Numerical studies* : The problem of colliding clouds has been studied numerically in the past for instance, by Stone (1970 a,b), Hausman (1981), Lattanzio *et al* (1985) and Hunter *et al* (1986); more recently by Bhattal *et al* (1998) and Klein & Woods (1998), among others. Stone (1970a) studied this problem in one dimension by simulating MCs as planes having infinite spatial extent and found that post-collision, the clouds coalesced and the resultant composite object then expanded. This experiment, in two dimensions yielded a result similar to the one dimensional case (Stone 1970b). Hausman (1981) performed particle simulations of head on and off centre cloud collisions. However, the results were corrupted due to particle penetration during collision.

Later Hunter *et al* (1986), in their grid simulation of colliding flows found that such collisions produced slabs which according to them were unstable to Rayleigh - Taylor like instability, but could not establish the exact nature of this instability. A similar conclusion was drawn by Stevens *et al* (1992) and Klein & Woods (1998). However, both found evidence for non linear growth of instabilities starting in thin shells within the slab. In fact the latter suggested occurrence of the non-linear thin shell instability (NTSI) in the shocked slab, resulting from cloud collisions. In this paper we demonstrate the occurrence of this instability in our SPH simulations of head-on cloud collision. The effect of numerical viscosity in SPH, on the growth rate of the NTSI is left for a future paper.

The plan of the paper is as follows. In §2 we briefly describe the SPH code employed for our cloud collision experiments. In §3 we discuss the procedure to set up initial conditions for the cloud collision experiments. In §4 we discuss the NTSI and simulation results and conclude in §5. The column density spans roughly eight orders of magnitude hence all column density plots presented here are plotted on a logarithmic scale. The column density is measured in  $M_{\odot} \text{pc}^{-2}$  and the distance in pc.

## 2 SMOOTHED PARTICLE HYDRODYNAMICS (SPH)

### 2.1 The SPH code used

All the simulations presented here have been performed using the DRAGON SPH code. It is a well tested code, the relevant details of which can be found in Goodwin, Whitworth & Ward-Thompson (2004). It uses the Barnes-Hut tree for gravity calculation ( $\theta_{crit} \sim 0.45$ ) and also includes quadrupole moments of remote cells. The forces are integrated using a second order Runge-Kutta integration scheme. Each particle has ( $50 \pm 5\%$ ) neighbours. The code employs a multiple particle time stepping scheme as against global time stepping and uses the standard form of artificial viscosity.

### 2.2 Brief description of the numerical scheme

SPH is a Lagrangian interpolation scheme, introduced by Gingold & Monaghan (1977) and Lucy (1977) to treat complicated problems in astrohydrodynamics. Under the scheme, the fluid being investigated is treated as an ensemble of a large number of particles or fluid markers. The particles in this case are not point masses in the strictest sense, but have a finite spatial extent. To understand this let us first consider the integral interpolant in three dimensional space.

*Interpolant and Kernel* : Consider an arbitrary function  $F(\mathbf{r})$ . The corresponding integral interpolant is

$$F_I(\mathbf{r}) = \int F(\mathbf{r}') \cdot W(\mathbf{r} - \mathbf{r}', h) d\mathbf{r}', \quad (1)$$

where the integration is performed over all space. The function  $W(\mathbf{r} - \mathbf{r}', h)$  is called the kernel and has the following two properties,

$$\int W(\mathbf{r} - \mathbf{r}', h) d\mathbf{r}' = 1 \quad (2)$$

and

$$\lim_{h \rightarrow 0} W(\mathbf{r} - \mathbf{r}', h) = \delta(\mathbf{r} - \mathbf{r}'). \quad (3)$$

The integration in equation (2) once again, is performed over all space. From equation (3), it can be seen that the kernel is non zero only within a finite region of space, having radius  $2h$ , called the kernel radius. In writing the integral interpolant, we envisage the fluid as an ensemble of little markers having finite extent (defined by the kernel radius) and contributing locally.

However, for numerical work it is convenient to replace the fluid markers with particles and the integral interpolant with a summation interpolant. The kernel then smoothes out discontinuities over individual particle contributions and the extent of a SPH particle is defined by its kernel radius. Various different choices of functions like the Gaussian, Heaviside step function and cubic splines, have been tried for the kernel. We use the standard M4 cubic spline,

$$W(\mathbf{r} - \mathbf{r}', h) = \frac{1}{4\pi} \begin{cases} 4 - 6s^2 + 3s^3 & , s \leq 1 \\ (2 - s)^3 & , 1 < s \leq 2 \\ 0 & , \text{otherwise;} \end{cases} \quad (4)$$

$s = \frac{r}{h}$ . However, at times artificial clumping has been observed because pairwise pressure between closely interacting particles goes to zero linearly. To avoid this, an alternative is to add a conservative, non zero repulsive force at small separations. This ensures a monotonic gradient of the kernel,

$$\frac{dW}{ds} = -\frac{1}{4\pi} \begin{cases} 4 & , s \leq \frac{2}{3} \\ 3s(4 - 3s) & , \frac{2}{3} < s \leq 1 \\ 3(2 - s)^2 & , 1 < s \leq 2 \\ 0 & , \text{otherwise} \end{cases} \quad (5)$$

(Thomas & Couchman 1992).

*SPH Density calculation and the gravity tree* : The SPH interpolation is performed using a summation interpolant, where the integral on the RHS of equation (1) is approximated by summation. The density of a single SPH particle is given by,

$$\rho_i \equiv \rho(\mathbf{r}_i) = \sum_{j=1}^{N_{neibs}} m_j \cdot W(\mathbf{r}_i - \mathbf{r}_j, h) \quad (6)$$

**Table 1.** List of simulations performed with relevant physical details.

| Serial No. | Experimental details   | $P_{ext}$ | Precollision Mach Number | Number of particles                     | Head on | EOS used |
|------------|--|-----------|--------------------------|---|---------|----------|
| 1          | $M_{cld1} = M_{cld2} = 100 M_{\odot}$<br>$R_{cld1} = R_{cld2} = 1 \text{ pc}$ , T = 84 K     | Yes       | 10                       | $N_{tot} = 34893$<br>$N_{gas} = 3516$   | Yes     | EOS-B    |
| 2          | $M_{cld1} = M_{cld2} = 50 M_{\odot}$<br>$R_{cld1} = R_{cld2} = 0.8 \text{ pc}$ , T = 54 K    | Yes       | 12                       | $N_{tot} = 129427$<br>$N_{gas} = 16000$ | Yes     | EOS-MOD  |
| 3          | $M_{cld1} = M_{cld2} = 150 M_{\odot}$<br>$R_{cld1} = R_{cld2} = 1.22 \text{ pc}$ , T = 104 K | Yes       | 35                       | $N_{tot} = 401569$<br>$N_{gas} = 40000$ | Yes     | EOS-MOD  |
| 4          | $M_{cld1} = M_{cld2} = 50 M_{\odot}$<br>$R_{cld1} = R_{cld2} = 0.8 \text{ pc}$ , T = 54 K    | No        | 12                       | $N_{gas} = 100000$                      | Yes     | EOS-MOD  |
| 5          | $M_{cld1} = M_{cld2} = 400 M_{\odot}$<br>$R_{cld1} = R_{cld2} = 2.0 \text{ pc}$ , T = 170 K  | Yes       | 13                       | $N_{gas} = 100000$                      | Yes     | EOS-MOD  |
| 6          | $M_{cld1} = M_{cld2} = 50 M_{\odot}$<br>$R_{cld1} = R_{cld2} = 0.8 \text{ pc}$ , T = 54 K    | No        | 13                       | $N_{gas} = 40000$                       | No      | EOS-MOD  |

Note : The numbers on the left hand side below indicate the respective column numbers of the table.

- (2) Physical details of individual clouds in a simulation.
- (3) Indicates if ICM particles were invoked in a simulation.
- (4) Precollision Mach number.
- (5) Total number of particles ( $N_{tot}$ ) used in a simulation (ICM + GAS). The number of gas particles ( $N_{gas}$ ) are separately mentioned.
- (6) Indicates if the clouds were allowed to collide head on/off centre.
- (7) The choice of EOS used (EOS-B & EOS-MOD correspond to equations (28) & (29), respectively).

where  $j$  is the identifier of the nearest neighbours of the particle  $i$  within its kernel radius and  $N_{neibs}$  is the number of neighbours desired. If the smoothing length,  $h$  is constant, we can integrate the density over the entire volume and obtain the total mass of the system,  $M$ ,

$$\int \rho(\mathbf{r}) d\tau = \sum_i m_i = M. \quad (7)$$

Thus, the total mass is conserved. In case  $h$  is allowed to vary spatially, then the above integral is not exactly equal to  $M$ , but the mass is still conserved since it is carried by particles.

The search for nearest neighbours of a particle can be performed using either the *gather* or the *scatter* scheme (Hernquist & Katz 1989). The SPH code DRAGON employs a hybrid combination of the two neighbour finding schemes. The net gravity acting on a single particle due to rest of the particles in the computational domain can be easily calculated by a brute force summation. However, this simple calculation is computationally expensive and hence, unfeasible. The force calculation can be considerably speeded up with the help of a gravity tree which is an approximation to the direct summation (Barnes & Hut 1986; Hernquist 1987; Hernquist & Barnes 1990).

According to this scheme, particles in the computational domain are distributed hierarchically in cells. The gravity on a single particle is calculated by treating remote cells as extended point masses. Better accuracy of the calculation demands that higher order moments of the cells also be included. Contributions from particles belonging to nearby cells are summed by brute force. The degree of closeness/remoteness of a cell from a particular particle is governed by a parameter called the cell opening angle,  $\theta$ , which is the angle subtended by the cell at the particle and  $\theta_{crit}$  is

a predefined critical value of this parameter. Cells qualifying the criterion  $\theta < \theta_{crit}$  are treated as extended point masses. The gravitational force between particle pairs with vanishingly small separations tends to infinitely large values due to the singular nature of Newtonian gravity. This problem is tackled using a gravitational kernel analogous to the density kernel. Like the density kernel,  $W(\mathbf{r} - \mathbf{r}', h)$ , the gravity kernel is also compact (Hernquist & Barnes 1990; Dehnen 2001).

*Artificial Viscosity* : Flow in real fluids is dissipative due to shearing motion between fluid layers. In SPH, artificial viscosity (AV) provides this dissipative mechanism and plays vital role in capturing shocks. Without AV, SPH particles would simply penetrate through each other. The SPH equation of motion for the  $i^{th}$  particle is

$$\frac{d\mathbf{v}_i}{dt} = - \sum_{j=1}^{N_{neibs}} m_j \left( \frac{P_j}{\rho_j^2} + \frac{P_i}{\rho_i^2} + \Pi_{ij} \right) \cdot \nabla_i W_{ij}, \quad (8)$$

where

$$\Pi_{ij} = \begin{cases} \frac{-\alpha \bar{a}_{ij} \mu_{ij} + \beta \mu_{ij}^2}{\bar{\rho}_{ij}} & , \mathbf{v}_{ij} \cdot \mathbf{r}_{ij} < 0; \\ 0 & , \mathbf{v}_{ij} \cdot \mathbf{r}_{ij} > 0; \end{cases} \quad (9)$$

and the shock term,

$$\mu_{ij} = h_{ij} \frac{\mathbf{v}_{ij} \cdot \mathbf{r}_{ij}}{|\mathbf{r}_{ij}|^2 + \eta^2}, \quad (10)$$

$\mathbf{r}_{ij} = \mathbf{r}_i - \mathbf{r}_j$ ,  $\mathbf{v}_{ij} = \mathbf{v}_i - \mathbf{v}_j$ . The first component of  $\Pi_{ij}$  produces shear and bulk viscosity, while the second term becomes important in strong shocks. This latter component is similar to the Von Neumann - Richtmeyer viscosity used in finite difference schemes (Monaghan 1992; Lattanzio *et al* 1985).

*Time stepping* : The time step is calculated using three criteria viz. the Courant condition, the viscosity condition

and the net force (per unit mass) condition, respectively. Thus the three choices of the time step for the  $i^{th}$  particle are,

$$\delta t_c = \min_i \left( \frac{h_i}{a_i} \right) \quad (11)$$

$$\delta t_v = \min_i \left( \frac{h_i}{a_i + 0.6(\alpha a_i + \beta \max_j \mu_{ij})} \right) \quad (12)$$

$$\delta t_F = \min_i \left( \frac{h_i}{|\mathbf{F}_i|} \right)^{1/2}, \quad (13)$$

(Monaghan 1992). The  $i^{th}$  particle is then assigned the time step,

$$\delta t_i = 0.02 \cdot \min(\delta_c, \delta_v, \delta_F).$$

The premultiplier in the expression above is to ensure stability of the integration scheme.

This is called the global time stepping scheme. The scheme, however becomes unsatisfactory once condensations start forming, i.e. when the smoothing length starts decreasing. As a natural consequence of the time stepping equations (11), (12) and (13), the corresponding time step also becomes small. To overcome this difficulty we implement the multiple particle time stepping scheme, according to which particles are assigned block time steps, which in turn are ordered in a hierarchy of powers of 2 (McMillan & Aarseth 1993).

*The sink particle* : Extremely dense agglomeration of particles in the computational domain is replaced by a *sink*. The concept of a sink particle was first introduced in SPH by Bate *et al* (1995). The rest of the gas particles interact with the sink only through gravity. SPH particles coming within a predefined radius, called the sink radius ( $R_{sink}$ ), are accreted by it, provided particles being accreted by the sink satisfy certain criteria (Bate *et al* 1995). In all the simulations presented here, the sink density is held fixed at  $\rho_{sink} = 10^{-12} \text{g cm}^{-3}$ , the second predefined parameter of a sink.  $R_{sink}$  is so chosen that the initial sink mass,  $M_{sink}$ , is comparable to the minimum resolvable mass in the simulation,  $M_{min}$ . Now,

$$M_{min} = N_{neibs} \cdot m_i$$

where  $m_i = \frac{M_{cld}}{N_{SPH}}$  and  $M_{sink} = \frac{4}{3}\pi R_{sink}^3 \rho_{sink}$ . In view of the above mentioned requirement,

$$R_{sink} \sim \left( \frac{N_{neibs} M_{cld}}{4 N_{SPH} \rho_{sink}} \right)^{1/3}.$$

In the present work, the sink particle represents a protostellar core.

### 3 NUMERICAL EXPERIMENTS PERFORMED

#### 3.1 Setting the initial conditions (ICs)

We first describe the scheme to assemble particles within a MC. We model a MC as simple external pressure confined isothermal spheres. If  $\xi$  is the dimensionless radius of the sphere, we choose a sphere of size  $\xi \equiv \xi_B = 3$ . The stability analysis of the isothermal sphere suggests that only spheres with radius smaller than the critical radius,  $\xi_{crit} = 6.45$ , can stay in equilibrium (Chandrasekar 1939). Thus, our choice of  $\xi_B$  ensures that the sphere is stable against self gravity.

For simplicity we further assume that the sphere contains only molecular hydrogen and if  $\bar{m}$  is the mean molecular mass of a gas particle, then the isothermal sound speed  $a_0$  is defined as

$$a_0 = \left( \frac{k_B T}{\bar{m}} \right)^{1/2}. \quad (14)$$

Here  $k_B$  and  $T$  respectively, are the Boltzmann constant and uniform gas temperature in the sphere.

The mass interior to this sphere,  $M(r_B)$ , is

$$M_{sphere} \equiv M(r_B) = 4\pi R_0^3 \rho_c \left( \xi^2 \frac{d\psi}{d\xi} \right)_{\xi_B}, \quad (15)$$

where  $\psi(\xi)$  is called the Emden function (Chandrasekar 1939) and the physical radius of the sphere,  $r_B = R_0 \xi_B$ ,  $R_0$  having the dimension of length is a distance scale factor, and defined as

$$R_0 = \frac{a_0}{(4\pi G \rho_c)^{1/2}}. \quad (16)$$

Taking the ratio of  $M_{sphere}$  with  $r_B$  we get,

$$\begin{aligned} \frac{M_{sphere}}{r_B} &= \frac{a_0^2 \mu(\xi_B)}{G \xi_B} \\ \Rightarrow a_0^2 &= \frac{G M_{sphere} \xi_B}{r_B \mu(\xi_B)}, \end{aligned} \quad (17)$$

where we define

$$\mu(\xi_B) = \left( \xi^2 \frac{d\psi}{d\xi} \right)_{\xi_B}.$$

The functions  $\psi(\xi)$  &  $\mu(\xi)$  are tabulated by integrating the isothermal Lane - Emden equation. The temperature within the sphere is fixed by using equations (14) and (17).

We position particles randomly in this sphere using three random number generators, each producing a random number in the range (0,1). A random number  $\mathcal{R}_r$  is chosen such that

$$\begin{aligned} \frac{M(r)}{M_{sphere}} &= \frac{\mu(\xi)}{\mu(\xi_B)} \equiv \mathcal{R}_r \\ \Rightarrow \mu(\xi) &= \mu(\xi_B) \mathcal{R}_r, \end{aligned} \quad (18)$$

Knowing the RHS of equation (18), the corresponding dimensionless radius  $\xi$  can be obtained from the Lane - Emden table. The radial distance  $r$  at which a particle is positioned within the sphere is then given by  $r = \mathcal{R}_r \xi$ . Then, the probability that a particle will lie in an infinitesimal interval of the poloidal angle ( $\theta$ ) and ( $\theta + d\theta$ ) is,

$$p_\theta d\theta = \frac{\sin \theta}{2} d\theta.$$

The total probability over the range of the angle  $\theta$  is,

$$P(\theta) = \int_{\theta'=0}^{\theta'=\theta} \frac{\sin \theta'}{2} d\theta' = \frac{1 - \cos \theta}{2} \equiv \mathcal{R}_\theta, \quad (19)$$

where  $\mathcal{R}_\theta$  is the second random number. Thus,

$$\cos \theta = 1 - 2\mathcal{R}_\theta,$$

and finally the azimuthal angle,  $\phi$ , of a particle is fixed as,  $\phi = 2\pi \mathcal{R}_\phi$ ;  $\mathcal{R}_\phi$  being a third random number. The  $(r, \theta, \phi)$  coordinates are then converted to their cartesian form in the usual way.

The density of this sphere is

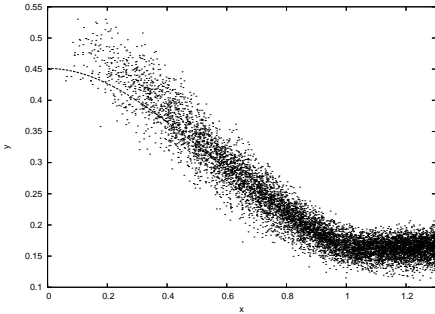


**Figure 1.** This figure shows the SPH density ( $\rho_{SPH}$ ) of the truncated isothermal sphere ( $\xi_B=3$ ). The dashed continuous line is the expected density profile ( $\rho(r)$ ) for this sphere. ( $x \equiv \xi$ ,  $y \equiv \rho_{SPH}$ ),  $N_{sphere} = 1500$ .

$$\rho(r) = \frac{a_0^6}{4\pi G^3 M_{sphere}^2} \left( \xi^2 \frac{d\psi}{d\xi} \right)_{\xi=\xi_B}^2 \cdot e^{-\psi(\xi_B)}, \quad (20)$$

and  $\xi_B = 3$  in the present case. Such a sphere in isolation will simply diffuse away and therefore needs to be spatially confined with a finite external pressure,  $P_{ext}$ , acting on its boundary. The magnitude of this pressure is

$$P_{ext} = \frac{a_0^8}{4\pi G^3 M_{sphere}^2} \cdot \mu(\xi_B) e^{-\psi(\xi_B)}, \quad (21)$$

where all symbols have their usual meanings (Chandrasekar 1939).

We simulate the warm external intercloud medium (ICM) by assembling particles in an envelope of finite thickness ( $\eta h_B$ ). Here  $h_B$  is the average smoothing length of a single SPH particle and  $\eta$  is a non zero integer defining the thickness of the envelope. Particles in this envelope interact with the gas particles within the cloud only by exerting hydrodynamic pressure of magnitude  $P_{ext}$ , defined by equation (21) above.

To avoid diffusion of particles across the cloud-ICM interface, care must be taken to avoid a gradient in particle number density. To ensure this, we first calculate the particle number density,  $\hat{n}_B$ , near the cloud edge and then evaluate the number of particles to be assembled in this envelope,  $N_{env}$ . For the purpose, we first obtain the expression for density at the cloud edge in its dimensionless form,  $\hat{\rho}_B$ . A trivial mathematical manipulation of equation (20) yields,

$$\hat{\rho}_B = \frac{\xi_B^3 e^{-\psi(\xi_B)}}{4\pi \mu(\xi_B)}. \quad (22)$$

The particle number density at the edge of the sphere is  $\hat{n}_B = \frac{\hat{\rho}_B}{m_i} \equiv N_{SPH} \hat{\rho}_B$ , where  $m_i$ , the mass of the  $i^{th}$  particle in our test sphere is  $m_i = \frac{1}{N_{SPH}}$  and the volume of the ICM envelope is  $\frac{4\pi[(1+\eta \cdot h_B)^3 - 1]}{3}$ , for a sphere of  $1 M_\odot$ . The number of particles to be assembled in the envelope,  $N_{env}$ , is then the product of this volume with the particle number density,  $\hat{n}_B$ .

The radial coordinate,  $r$ , of a particle in the envelope is fixed by choosing a random number  $\mathcal{R}_r$  such that the volume interior to this radius is proportional to the volume in the envelope i.e

$$\mathcal{R}_r = \frac{(r^3 - 1)}{((1 + \eta h_B)^3 - 1)}.$$

The polar angles ( $\theta, \phi$ ) of individual particles are determined as before. The polar coordinates of particles are then converted to their cartesian form. With this, the assembly of the sphere - envelope system is completed.

To test this scheme of assembling particles, we assemble 1500 particles within the sphere ( $N_{SPH}$ ) and with a choice of  $\eta = 5$ ,  $N_{env} = 6159$ . This assembly of the sphere - envelope combine is then placed in a periodic box and allowed to evolve. The periodic box is simply meant for ghosting particles i.e. particles leaving from one face of the cube re-enter from the opposite face. The assembly is suitably heated for a fraction of the sound crossing time. Fig. (1) shows the SPH density after about half sound crossing time and seems to be in reasonable agreement with the expected density profile, marked by the dashed continuous curve.

The box of the ICM particles is set up in a manner similar to the envelope of  $P_{ext}$  particles for the truncated isothermal sphere, described above. The dimensions of the box are so set that each sphere has an envelope of thickness of  $3h_B$ . Fig. (2) below shows a schematic diagram of the initial set up. It is a two dimensional picture showing the precollision MCs, barely touching each other. The circles drawn with continuous lines represent the precollision individual clouds. Each one of these circles is circumscribed by respective dashed circles. These latter circles show the extent of the ICM envelope for each cloud.

Since we have opted to use physically identical clouds, each one of them has the same mass,  $M_{cld}$ , radius,  $R_{cld}$ , and an envelope of the ICM particles of thickness  $\eta h_B$ . The length of the ICM box along the axis of collision (the  $x$  axis in Fig. (2)) is

$$x = 4(R + \eta h_B),$$

while that along the  $y$  and  $z$  axes respectively, is

$$y = z = 2(R + \eta h_B),$$

and  $\eta = 3$  in the present case. A short coming of our SPH code is that it requires a cubic periodic box. Each side of the cubic box therefore has length  $x$  pc.

Let  $N_{SPH1}$  and  $N_{SPH2}$  be the number of gas particles in each cloud (provided externally). The number of particles to be assembled in the ICM envelope of respective spheres is  $N_{env1}$  and  $N_{env2}$ . The region marked by stripes in Fig. (2) is that occupied by the ICM particles. The volume of this region can be trivially calculated. We also know the required particle density,  $\hat{n}_B$ , in this region using which the number of particles to be assembled in this region is calculated. The total number of particles in the box is simply the sum of  $N_{SPH1}$ ,  $N_{SPH2}$ ,  $N_{env1}$ ,  $N_{env2}$  and the number of ICM particles in the striped region of the box.

Particles in this box are assembled on a HCP lattice. Particles within the desired cloud radius are then scooped out and replaced with corresponding gas particles. The second cloud is assembled in a similar manner. This concludes the process of setting up the ICs.

### 3.2 Models tested

The cloud collision experiments performed by us have been listed in Table (1) above. The table provides the relevant physical details of an experiment. For an arbitrary choice of the cloud mass,  $M_{cld}$ , the corresponding cloud radius,  $R_{cld}$ ,

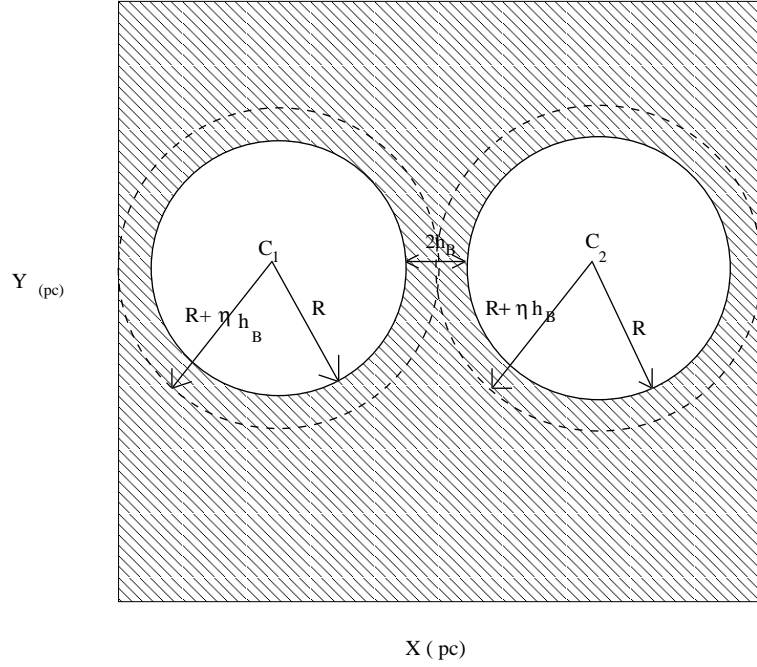


**Figure 2.** Schematic diagram of the initial set up of colliding clouds. See text above for description.

is determined using the Larson's scaling relation between mass and radius,

$$R_{cld}(\text{pc}) = 0.1 \text{pc} \left( \frac{M_{cld}}{M_{\odot}} \right)^{0.5}. \quad (23)$$

### 3.3 Equation of state

We make use of two different choices of the equation of state (EOS). The first choice is that of a simple barotropic EOS given by,

$$\left( \frac{T}{\text{K}^{\circ}} \right) = \left( \frac{T_0}{\text{K}^{\circ}} \right) \left[ 1 + \left( \frac{\rho}{10^{-14} \text{g cm}^{-3}} \right)^{\gamma-1} \right]. \quad (24)$$

Here  $T_0$  is the ambient temperature,  $\rho$  the gas density and  $\gamma$  is the polytropic constant which, in the non-relativistic case is  $\frac{5}{3}$ . This EOS flips from being isothermal ( $T \sim T_0$ ) to adiabatic at a critical density of  $\sim 10^{-14} \text{g cm}^{-3}$ . In the adiabatic regime  $T \propto \rho^{\frac{2}{3}}$ .

The second choice of the EOS is,

$$\left( \frac{T}{\text{K}^{\circ}} \right) = \left( \frac{T_0}{\text{K}^{\circ}} \right) \left[ (2.1 \times 10^{-19}) \cdot \left( \frac{\rho}{\text{g cm}^{-3}} \right)^{-1} + 1 + (2.4 \times 10^{10}) \cdot \left( \frac{\rho}{\text{g cm}^{-3}} \right)^{\frac{2}{3}} \right] \quad (25)$$

According to this EOS, initially the temperature,  $T$ , decreases as  $\rho^{-1}$  up to  $\rho \sim 10^{-19} \text{g cm}^{-3}$ , then remains constant at  $\sim 10 \text{K}$  in the range  $\rho \in (10^{-19}, 10^{-15}) \text{g cm}^{-3}$  and finally as the density increases beyond  $\sim 10^{-15} \text{g cm}^{-3}$ , the EOS mimics equation (24). Thus, the EOS has three regions in the  $T - \rho$  space as can be seen from Fig. (3). Each of the three regions are marked by numbers 1, 2 and 3 respectively. The first region is dominated by radiative cooling, the second (flat) region is where approximate isothermality

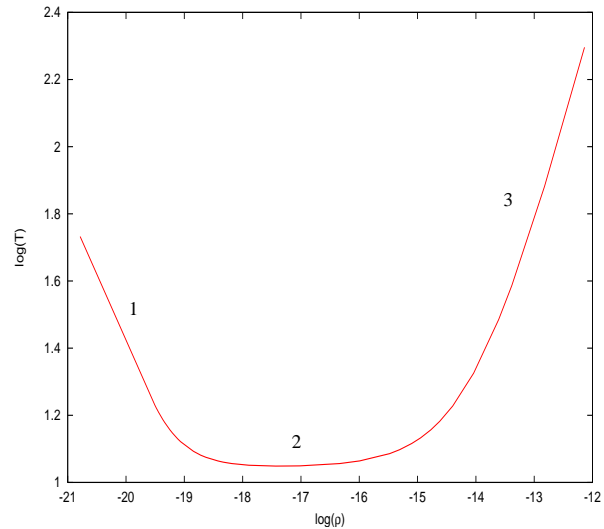


**Figure 3.** The  $T - \rho$  space for the modified EOS. Temperature ( $T$ ) is measured in degree Kelvin and density ( $\rho$ ) in  $\text{g cm}^{-3}$ .

is maintained and the third corresponds to adiabatic heating. A detailed derivation of this EOS can be found in Low & Lynden - Bell (1976).

With this choice of the EOS, the precollision clouds start at the top of region 1 in Fig. (3) and then subsequently slide down along the  $\log(T) - \log(\rho)$  characteristic. Post-collision, a dense shock compressed layer is formed and a strongly radiating shock maintains approximate isothermality in the slab. Regions in the slab which are dense enough, have temperatures  $\sim 10 \text{K}$  as can be seen from Fig. (3). This is however, a very simplified treatment of radiative cooling

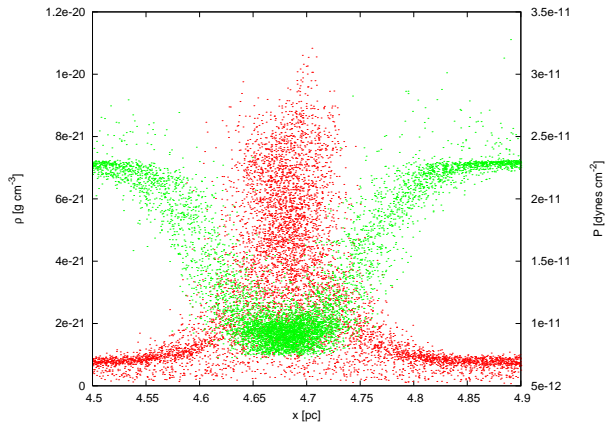


**Figure 4.** Plot of  $\rho$  (red dots) and  $P$  (green dots) against distance in the  $x$  direction for model 4. See Table (1) for physical details of the clouds.

that may occur through a variety of mechanisms like molecular emission, recombination line emission or collisional emission. We would like to improve upon our simulations by employing a more rigorous treatment of radiative cooling.

## 4 DISCUSSION

### 4.1 Observations from experiments performed

The problem of growth of instabilities in a cold, isothermal slab has been thoroughly investigated in the past. Linear perturbative analyses have shown the existence of various unstable modes, see for instance Ledoux (1951), Chandrasekhar (1953), Mestel (1965) and Simon (1965). However, these investigations assumed slabs with no external forces acting on them.

Growth of instabilities in shock compressed slabs was first studied by Vishniac (1983) by invoking full shock conditions and found evidence for the existence of bending modes of the shocked slab. His linear analysis of the growth of these bending modes suggested that the instability became overstable and led to disintegration of the slab. In this regime gravitational instabilities are suppressed. The bending modes of the slab are amplified due to the difference between external ram pressure acting on the slab and internal thermal pressure of the slab. In the perturbed regions of the slab, there is a net imbalance between the two types of pressure and the perturbation continues to amplify.

This investigation was extended by Vishniac (1994) to the non-linear regime to investigate bending as well as breathing modes of such a slab. He showed that an isothermal shock compressed slab of inviscid fluid became unstable to non-linear growth of shearing instability. Since this instability commences in thin shells (i.e. between layers of the slab), it is called the Non-linear Thin Shell Instability (NTSI). The instability grows rapidly and saturates leading to turbulent mixing between layers of the slab. The slab eventually forms a sieve like structure and finally disintegrates to form a filament aligned along the collision axis. Gravitational clustering can then occur in this filament.

When the colliding clouds first touch each other, they

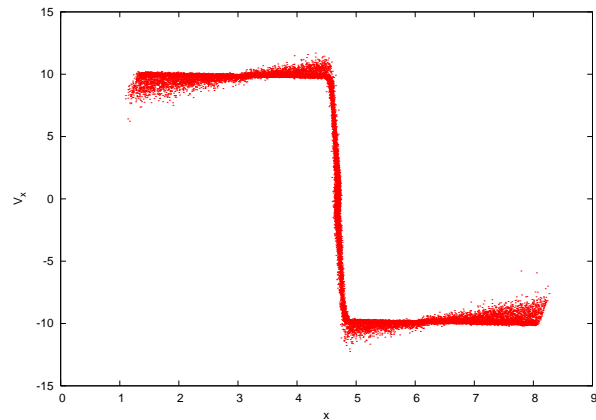


**Figure 5.** Plot of the post shock jump in the  $x$  component of velocity against the distance in  $x$  direction for model 4. The epoch for this plot is the same as that for Fig. (4).

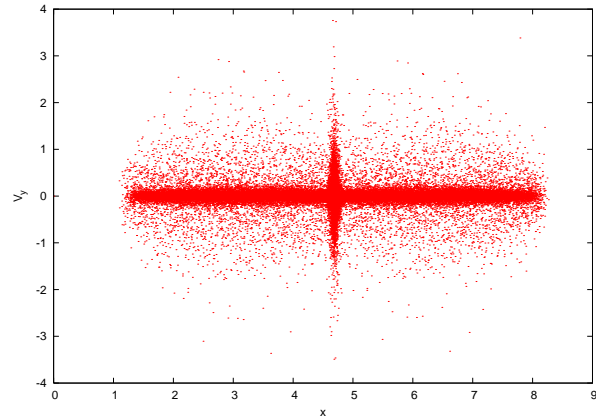


**Figure 6.** Plot of the post shock  $y$  component of velocity against the distance in  $x$  direction for model 4. The epoch for this plot is the same as that for Figs. (4) and (5). We can see that post collision, there is supersonic transverse velocity component

form a contact discontinuity. Subsequently, individual clouds collapse and form a shock compressed slab. The time required for the collapse of a cloud is called the cloud crushing time,  $t_{cr}$  (Klein & Woods, 1998). After the formation of the initial shock front, the shock wave propagates through the cloud and reaches the far edge, in a time  $t_{cr} \sim \frac{2R_{cld}}{v_s}$ , where  $R_{cld}$  is the cloud radius and  $v_s$  is the velocity of the shock wave.

The post-collision contact discontinuity indeed becomes unstable and can be seen in the following way. Fig. (4) shows a plot of density and total pressure (thermal + ram) just after the shock formation in model 4 (see Table (4.1)). The figure shows that the gradient of the two quantities have opposite signs at the surface of the contact discontinuity. All models showing evidence for the NTSI, employ the modified EOS as defined by equation (25). These models are characteristically different compared to model 1.

The sudden drop in the total pressure across the discontinuity is the result of a transition from being isotropic, thermal pressure (at the contact discontinuity), to being ram

pressure on the outer surface of the discontinuity. As a result, the interface between the slab surface and material being freshly accreted may become unstable. Unlike Hunter *et al* (1986), we are however, disinclined to term this situation as Rayleigh-Taylor (RT) unstable.

Figs. (5) and (6) show respectively, the profiles of the  $x$  and  $y$  components of velocities against distance in the  $x$  direction. The formation of a stationary contact discontinuity is evident from Fig. (5). On the other hand, from Fig. (6) we can see that the gas colliding with the contact discontinuity has a supersonic (relative to the local sound speed in the slab) transverse velocity component. The contact discontinuity is smeared due to the SPH artificial viscosity.

The strong shear between adjacent layers makes the slab layers Kelvin-Helmholtz (KH) unstable. With the help of first order perturbative analysis, it can also be shown that fluid surfaces in shearing contact develop surface gravity waves which give them a rippled appearance, called the breathing modes of the fluid surface. This situation is analogous to the formation of ripples on the surface of water in water bodies (Raichaudhari 1999; Shore 2007). Fig. (10) below shows a face-on view of the shocked slab formed in model 2. It shows a network of filamentary structure, clump ( $\rho \sim 10^{-18}$  g cm $^{-3}$ ) formation is visible in regions where filaments intersect, however this structure suffers from tidal disruption due to strong shearing motion between slab layers. Klessen & Burkert (2000) for instance, make similar observations about clump formation in their turbulence models of the GMC interiors.

Model 1 tested here is a low resolution test and employs a barotropic EOS. Post-cloud collision, a dense composite object is formed. In this case, AV is the only dissipative mechanism, but is insufficient to counter the rapid post-shock heating. Consequently this composite object simply re-expands. From equation (24), it follows that this object does not radiate heat and therefore has a higher Jeans mass. We therefore do not observe any evidence for growth of gravitational instabilities.

## 4.2 The NTSI

The problem under investigation here is that of the stability of a viscous fluid slab confined by accretion shocks on its either sides. The physical conditions leading to the occurrence of the NTSI have already been discussed in §4.1. As the slab accretes material, any small perturbations i.e. the bending modes of the slab get amplified due to non linear transfer of momentum within the slab.

There is a net deposition of positive momentum in those regions of the slab which are displaced upstream and a net deposition of negative momentum in regions displaced downstream, relative to the gas flow. This transfer of momentum amplifies the bending modes of the slab to scales greater than the thickness of the slab itself. It is essential to note that the pressure within the slab is thermal and isotropic while the external one is ram pressure. This distinction is irrelevant in the unperturbed state.

However, once a bending mode of the slab is excited, there is a net imbalance in forces acting on the convex and concave regions of the slab. In general, the accreted material converges in the convex regions of the slab and diverges in the concave regions. Slab layers undergo turbulent mixing

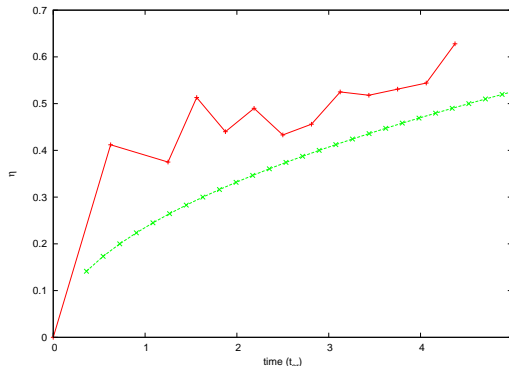


**Figure 7.** The growth rate of the NTSI in model 2. The red curve corresponds to the actual growth rate of NTSI in the simulation while the green curve is a power law fit (Eqn. (28)) to the observed growth rate. Time on the  $x$  axis is measured in units of the cloud crushing time  $t_{cr}$  defined above..

due to strong shear between them. If  $\tau$  is the dynamic time scale of the shocked slab (i.e. the time scale on which the physical properties of the slab evolve dynamically), turbulent mixing occurs when  $\tau$  is greater than the time required for the generation of the next similar layer at a distance greater than the wavelength and having wavenumber  $k$ . If  $L$  is the thickness of the slab and  $t$  is its age then,

$$\tau \gg \frac{t}{kL}, \quad (26)$$

(Vishniac 1994), is the condition under which turbulent mixing is suppressed.

If  $\tau \sim t$ , the turbulent mixing is weak and is only marginally effective in the post-shock slab. The turbulent mixing of slab layers gives rise to eddies on the scale of slab thickness which is an effective means of energy dissipation. Large scale turbulent motion within the slab immediately produces structure in it, but the density features are rapidly destroyed due to strong shear. In the limit of a small bending angle, linear analysis is sufficient to predict the growth rate of the unstable mode (Vishniac 1983). The linear theory however, breaks down when velocities within the slab become comparable to the local sound speed and fluctuations in column density become of order unity. The subsequent evolution of the instability becomes non-linear and the growth rate is,

$$\tau^{-1} \sim a_0 k (kx_m)^{1/2} \cdot C_d^{-1/2}, \quad (27)$$

(Vishniac 1994).

Here  $x_m$  denotes the mid-plane of the slab and  $C_d$  is a constant of order unity. This constant describes the extent of dissipation resulting from mixing between slab layers due to KH instability. Klein & Woods (1998) estimate  $2 \lesssim C_d \lesssim 4$  and a rate of saturation  $> a_0 k (kL)^{1/2}$ . Linear analysis by Vishniac (1983) suggested that the thin shell instability leads to fragmentation of the shock front. The resulting fragments are gradually eroded due to RT instability.

Below we first discuss model 2 (see Table (1)) as a representative case of head-on cloud collision and then other cloud collision models of this type. In §4.5 we discuss model 6, the

only off-centre cloud collision model tested in the present work.

### 4.3 The instability observed in the simulations

#### Model 2

Snapshots in Fig. (9) show the collision between clouds and the formation of a shocked slab. The slab then develops a kink on it (the bending of the slab). This can be seen in the picture on the right hand side of Fig. (9) ( $t = 0.2$  Myr). Soon after the formation of the shocked slab, we observe structure formation on its surface as is evident from Fig. (10). This is the result of various breathing modes of the slab. Shearing motion between slab layers is responsible for the KH instability, whose distinct feature is vortex formation. The right hand picture in the top panel of Fig. (12) shows the existence of circular velocity fields in the slab. During subsequent evolution of this slab a few breakaway blobs are visible near its edges, as can be seen from the pictures of the slab (see Figs. (11) and (12)).

This is perhaps due to the inability of SPH in its simplest form to model the KH instability, apparently due to formation of artificial boundaries between regions having steep density contrast (Agertz *et al* 2007). This problem can be fixed by including some additional correction terms to account for thermal energy dissipation across these boundaries (Price 2007). Our code does not include these corrections, however this shortcoming does not seem to have any adverse bearing on the results of the simulations and in any case it is not our aim here, to model the KH instabilities in their minute details.

At this point, we note that similar breakaway blobs, having much smaller densities (at least by two orders of magnitude), as compared to those observed in our simulations, have been reported by Heitsch *et al* (2008). They interpret this observation as evidence for core formation. Contrary to their conclusion, we discount the blobs as numerical artifacts despite they having densities as high as  $\sim 10^{-18}$  g  $\text{cm}^{-3}$ . However, we do observe structure formation in the shocked slab as can be seen in Fig. (10). If we relax our scepticism pertaining to these blobs, then it implies that core formation can occur even when the NTSI dominates the slab behaviour. However, these cores are too turbulent and do not collapse under self gravity.

Dense clumps form in regions where the filaments merge, but do not undergo gravitational collapse as they either suffer tidal disruption or merge with other clumps to form larger clumps. As the slab grows older, it disintegrates and collapses under self gravity to form a thin filament with a large aspect ratio, along the axis of collision. Gravitational clustering occurs in this filament and over a period of  $\sim 10^5$  yrs, eight sinks form in it. The pictures at time  $t=0.5$  Myr,  $0.75$  Myr, and  $1.0$  Myr respectively show the collapsing slab, while formation of the filament can be seen in the bottom panel of Fig. (11). The sinks have been marked by thick purple dots in the snapshot corresponding to  $t=1.52$  Myrs (see Fig. (11)).

By measuring the amplitude of the perturbation and the slab thickness, we estimate the growth rate of the NTSI as

$$\tau^{-1} \sim 0.5(kL)^{0.81}, \quad (28)$$

where symbols have their usual meanings. This is in excellent agreement with that predicted by Blondin & Marks (1996) and Klein & Woods (1998). They suggest,  $\tau^{-1} \sim 0.4(kL)^{0.7}$ . The growth rate of the NTSI observed by us and the former authors however, does not match with that proposed by Vishniac (1994), given by equation (27) above. This later equation predicts a much faster growth ( $k^{1.5}$ ), of the instability. This is presumably the result of his assumption of an inviscid fluid. Fig. (7) above shows the growth rate of the NTSI observed in model 2. The red curve corresponds to the actual measurement while the smooth, green curve is a power law fit corresponding to equation (28). The bracketed quantity in this equation is denoted as  $\eta$  in Fig. (7).

Fig. (8) is a plot of particle positions in the  $xy$  plane. The filament with eight sinks embedded in it can be clearly seen in this plot. Each sink has its respective protostellar disk perpendicular to the filament. Under the premise that outflows have small opening angles (in other words outflows are roughly aligned with the direction of the angular momentum vector of the matter being accreted by the YSO), outflows from YSOs having their disks orthogonal to the parent filament would be aligned with the filament. Perhaps, the process leading to filament formation has a crucial role to play in the orientation of protostellar disks relative to their natal filament.

Anathpindika & Whitworth (2008) surveyed five nearby, low mass filamentary star forming regions and suggested that outflows from YSOs embedded in filaments are distributed about a direction orthogonal to the filament. The results of our simulations presented here are apparently in contradiction with their conclusion.

### 4.4 Other head-on cloud collision models

The features of the NTSI discussed above, are evident in models 3, 4 & 5. Figs. (13) and (14) below, show a close-in view of the shock compressed slab in models 3 and 5 respectively. Overlaid on them, is the local velocity field to facilitate identification of the complicated fluid flow patterns resulting from turbulent mixing between slab layers. The top panel in Fig. (13) for instance, shows that the instability starts as a small perturbation on the shocked slab. Subsequently the slab accretes material from collapsing clouds which then excites other bending modes of the slab.

In model 5 we do not invoke the ICM, instead increase the number of gas particles to improve resolution. Snapshots in Fig. (14) show oscillations of the resultant shocked slab. The features of the NTSI are visible in all the pictures of this figure. Immediately after cloud collision, we observe gas squirting out from the upper and lower ends of the shocked slab, in all the models under this category. See Figs. (9) and (11) for example, corresponding to model 2.

Various features observed in model 2 and discussed in §4.3, are also seen in the remaining models described in this subsection. Barring model 3, we terminated the computation in models 4 and 5 shortly after the filament formation. In model 3, we observe that the sink formation in the filament commences rather early as compared to that in model 2. Sink formation in this model is observed after  $t = 0.77$  Myr, which in case of model 2 was observed after  $t \sim 1.45$  Myrs. The resulting slab in model 3 is much more massive than that in

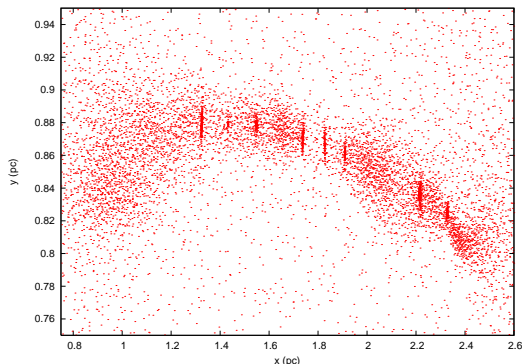


**Figure 8.** A plot of particle positions showing the filament formed in model 2. Eight sinks with their respective accretion disks are clearly visible. Observe that the disks are perpendicular to the filament.

model 2, due to which the wavelength of the gravitational instability is shorter and its growth rate, larger.

Similar to model 2, the gravitational clustering commences only after turbulence has sufficiently dissipated through post-shock mixing between slab layers, during which the slab has already collapsed under self gravity to form a thin filament with a large aspect ratio along the collision axis. As in model 2, the sinks are observed to have circumscribing protostellar disks oriented orthogonal to their natal filament.

#### 4.5 Off-centre cloud collision

##### model 6

We have tested one off-centre cloud collision model here. In this model the clouds are allowed to collide at a finite impact parameter,  $b = \frac{R_{cld}}{4}$ . The high velocity cloud collision in this case, produces an oblique shock compressed slab. Unlike the planar slabs formed in the head-on collision, in the present case we observe that the slab has three distinct regions. The central planar region and the two arched extensions at the top and bottom ends of the slab. See snapshots in the panels of Fig. (15).

The oblique shocked slab has these extended features due to the fact that the initial shock front effectively blocks the fluid flow from either sides in the central regions, while at the top end where the fluid flows from the right to left, has higher transverse velocity compared to that in the central regions. For the same reason there is also an extension at the lower end of the slab, except that the fluid at this end is flowing from the left to right.

The slab is internally stressed and exhibits a non-uniform velocity field. There is strong shearing motion between slab layers which is responsible for the KH instability. In the top panel of Fig. (16) we can see the formation of well defined structure. The slab breaks up to form blobs, a few of which merge to form a network of filaments and larger clumps. We observe that the oblique shocked slab exhibits rotational motion about an axis orthogonal to the plane of collision ( $z$  axis).

The lower panel in Fig. (16) shows a close-in view of clumps undergoing merger. The slab dissipates thermal

support through internal shearing motion. Usami, Hanawa & Fujimoto (1995) provide a detailed analytic account of such oblique shock compressed slabs. They conclude that gravitational instabilities are suppressed in slabs dominated by shearing motion. Shearing motion increases the effective sound speed and therefore damps the growth rate of the gravitational instability.

They further predict that the end product of such slabs is an elongated object, similar to the one we observe at the end of this calculation. We terminated this calculation after a sink was formed in the filament. We note that the sink formation is delayed in this case as compared to the high velocity, head-on cloud collisions discussed in case I above. This is due to the additional support provided by the angular momentum associated with rotation of the slab. The first sink is formed after  $t \sim 1.92$  Myrs.

In particular we note that there is no evidence for the NTSI, which dominated the evolution of the shock compressed slab produced by the high velocity head-on cloud collision. The Coriolis force acting on the rotating slab in the present case tends to suppress perturbations normal to the slab surface, in other words the bending modes of the slab. Without perturbations on the slab surface, the NTSI cannot grow.

This is however, contrary to the findings of Whitworth *et al* (1995) where they simulated low velocity ( $\sim 1.6$  km  $s^{-1}$ ), off-centre cloud collisions. They found that sufficiently dense regions in the filament collapsed under self gravity and the collapsing region was fed with material channeled by the filament that resulted from cloud collision. The protostellar object continued to accrete matter through an accretion disk oriented orthogonal to the direction of angular momentum vector of the filament.

## 5 CONCLUSIONS

The evolution of turbulent fluids is much more complicated than a simple interplay between gravity and thermal pressure. Collision between MCs is an important problem in interstellar gas dynamics since it is one of the mechanisms of energy dissipation in the ISM and spawn star formation. It also allows us to understand the dynamics of colliding fluid flows in the ISM. Through such studies, we can study the role of shearing instabilities in astrophysical environments.

The feature of the instability observed in all our head-on cloud collision experiments presented here, resembles that of the non-linear thin shell instability (NTSI). Rapid amplification of small scale perturbations on the shocked slab is a distinct trait of the NTSI. Evidence of this instability has also been observed in recent simulations of colliding turbulent fluid flows, performed by employing a finite difference code (Heitsch *et al* 2008).

In this paper we have attempted to demonstrate that in case of strongly shearing fluid interfaces, gravitational instabilities are suppressed. This has been established analytically by Usami, Hanawa, Fujimoto (1995). MC collision has been investigated using SPH in the past, but there has been no evidence for shearing instabilities in the post collision slab. This could be the result of a stiff EOS, small pre-collision velocity of individual clouds or poor resolution due to the use of too few particles. It has generally been

reported that high velocity cloud collisions result in the formation of a compact object that re-expands, see for instance Hausman (1981) and Lattanzio *et al* (1985).

In the rest of our simulations, we have found that strongly radiating shocks result in the formation of a cold dense slab. We adopted a modified EOS to account for radiative cooling. However, for a more complete treatment of the problem, advanced cooling techniques need to be introduced (e.g. Koyama & Inutsuka 2000; Semadini *et al* 2007). As the individual colliding clouds collapse on the slab, some material is ejected from the upper and lower ends of the slab. The slab disintegrates and collapses to form a thin long filament with a large aspect ratio. Gravitational clustering is observed in this filament.

Our simulations show that layers of the shocked slab are in shearing contact and the slab is dominated by the NTSI. It collapses under self gravity after losing thermal support. This is similar to the observation made by Klein & Woods (1998); Heitsch *et al* (2008). The former additionally note that there is no evidence for this instability in case of adiabatic shocks as perturbations on the slab surface do not grow in to the non-linear regime. The adiabatic shocks do not dissipate post shock kinetic energy and therefore tend to rapidly re-expand on a timescale much shorter than that required for the growth of bending modes. The observation in our model 1 where the post-shock composite object simply re-expands, is in consonance with this argument.

We measure the growth rate of the NTSI only for model 2 since the nature of the shocked slab evolution in other head-on cloud collision models barring model 1, is similar to this case. The oblique shocked slab in model 6 is also internally stressed. Breathing modes develop on the slab surface but we observe no evidence of their further growth. Also, there is no evidence for growth of the NTSI in the oblique shocked slab although, the slab still evolves towards a thin, long filament (as in models 2, 3, 4 and 5) along the collision axis.

It is essential to investigate the effect of AV on growth rate of the NTSI. We adopted the standard AV in all our simulations here. The models presented here are extremely simple, since we have preferred to use physically identical clouds without any internal perturbations. Also, the treatment of radiative cooling is simplified. We have not included magnetic fields in the present investigation. It would be an instructive exercise to start with magnetised clouds and allow them to collide. We can then study the effect of magnetic field on the evolution of the shocked slab and in particular observe if the NTSI develops in this case.

## ACKNOWLEDGMENTS

Mr. Anathpindika thanks the State Government Of Maharashtra, India for the post graduate research funding (DSW/Edu/Inf/2004/6283(35)). I thank Dr. S. Goodwin for making available the latest version of his SPH code DRAGON. All the column density plots presented here have been prepared using the publically available graphics package, SPLASH prepared by Dr. D. Price (Price 2007).

## REFERENCES

- Agertz *et al*, 2007, MNRAS, 380, 963  
 Anathpindika, S. & Whitworth, A., 2008, A&A accepted  
 Barnes, J & Hut, P., 1986, Nature, 324, 446  
 Bate, M., Bonnell, I., Price, N., 1995, MNRAS, 277, 362  
 Bhattal, A., Francis, N., Watkins, S. & Whitworth, A., 1998, MNRAS, 297, 435  
 Blondin, J & Marks, B., 1996, New Astronomy, 1(3), 235  
 Chandrasekar. S., 1939, An Introduction To The Study Of Stellar Structure, Dover Pub.  
 Chandrasekhar. S., 1953, MNRAS, 113, 667  
 Chandrasekar. S., 1962, Hydrodynamic and Hydromagnetic Stability, Oxford Clarendon Press  
 Chini, R., Reipurth, B., Ward-Thompson, D., Bally, J., Nyman, L., Sievers, A. & Billawala, Y., 1997, ApJ, 474, L135  
 Dale, J., Clark, P. & Bonnell, I., 2007, MNRAS, 377, 535  
 Dehnen. W., 2001, MNRAS, 324, 273  
 Elmegreen. B., 1998, ApJ, 477, 196  
 Elmegreen, B., 2007, ApJ, 668, 1064  
 Fleck Jr.,R., 1992, ApJ, 401, 146  
 Gingold, R. & Monaghan, J., 1977, MNRAS, 181, 375  
 Goodwin, S., Whitworth, A., Ward-Thompson, D., 2004, MNRAS, 414, 633  
 Hatchell, J., Richer, J., Fuller, G., Qualtborough, C., Ladd, E. & Chandler, C., 2005, A&A 440, 151  
 Hausman. M., 1981, ApJ, 245, 72  
 Heitsch, F., Slyz, A., Devreindt, J., Hartmann, L. & Burkert, A., 2006, ApJ, 642, 1052  
 Heitsch, F., Hartmann, L., Slyz, A., Devriendt, J. & Burkert, A., 2008, ApJ, 674, 316  
 Hernquist, L., 1987, ApJSS, 64, 715  
 Hernquist, L. & Katz, N., 1989, ApJS, 70, 419  
 Hernquist, L. & Barnes, J., 1990, ApJ, 349, 562  
 Hunter, J., Jr., Sandford, M., II, Whitaker, R. & Klien, R., 1986, ApJ, 305, 309  
 Johnstone, D. & Bally, J., 1999 ApJ, 510, L49  
 Kaplan, S., 1966, Interstellar Gas Dynamics, Oxford Pergamon Press.  
 Klessen, R. & Burkert, A., 2000 ApJS, 128, 287  
 Klein, R. & Woods, D., 1998, ApJ, 497, 777  
 Koyama, H. & Inutsuka, S., 2000, ApJ, 532, 980  
 Larson, R., 1981, MNRAS, 194, 809  
 Lattanzio, J., Monaghan, J., Pongracic, H., & Schwarz, M., 1985, MNRAS, 215, 125  
 Ledoux, P., 1951, An. Ap., 14, 438  
 Lucy, L., 1977, Aj, 82, 1013  
 McLow, M. & Klessen, R., 2004, Rev. Mod. Phy., 76, 125  
 McMillan, S. & Aarseth, S., 1993 ApJ, 414, 202  
 Mestel, L., 1965, QJRAS, 161  
 Monaghan, J., 1992, An. Rev. AA, 30, 543  
 Nagai, T., Inutsuka, S. & Miyama, S., 1998 ApJ, 506, 306  
 Price, D., 2007, PASA, 24(3), 159  
 Price, D., 2007, astro-ph/ 0709.2772  
 Raichaudhari, A., 1999, The Physics Of Fluids And Plasmas, Cambridge University Press  
 Roberts, W., 1969, ApJ, 158, 123  
 Schneider, S. & Elmegreen, B., 1979, ApJS, 41, 87  
 Shore, S., 2007, Astrophysical Hydrodynamics, John Wiley Pub. Inc.  
 Simon, R., 1965, An. Ap, 28, 40  
 Solomon, P., Rivolo, A., Barrett, J., & Yahil, A., 1987, ApJ,

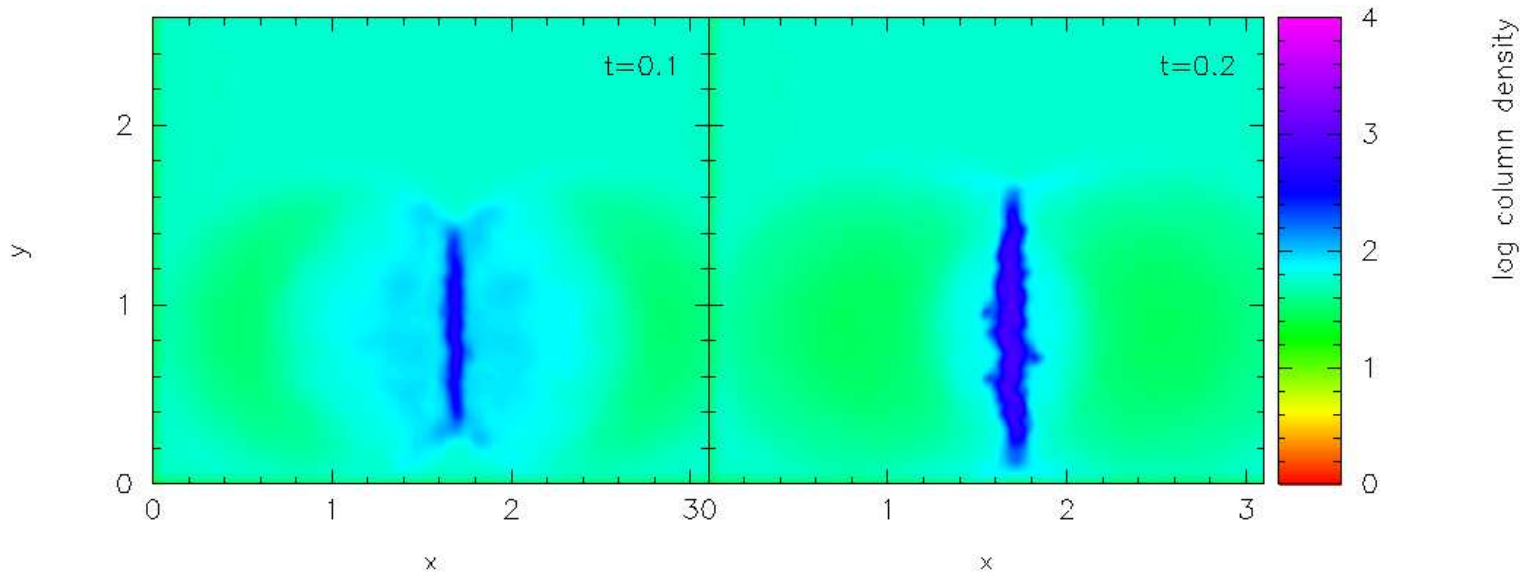


**Figure 9.** Formation of the shock compressed slab in model 2, time measured in Myrs. The bending mode of the slab can be seen in the right hand picture.

319, 730

Spitzer, L., 1968, *Nebulae & Interstellar Matter*, eds. Middlehurst, B & Lawrence, A., Chicago University Press, chap. 1

Stevens, I., Blondin, J. & Pollock, I., 1992, *ApJ*, 386, 265

Stone, M., 1970, *ApJ*, 159, 277

Stone, M., 1970, *ApJ*, 159, 293

Strickland, R. & Blondin, J., 1995, *ApJ*, 449, 727

Thomas, P. & Couchman, H. 1992, *MNRAS*, 257, 11

Usami, M., Hanawa, T. & Fujimoto, M., 1995, *PASJ*, 47, 271

Vázquez-Semadeni et al, 2007, *ApJ*, 657, 870

Vishniac. E., 1981, *ApJ*, 274, 152

Vishniac. E., 1994, *ApJ*, 428, 186

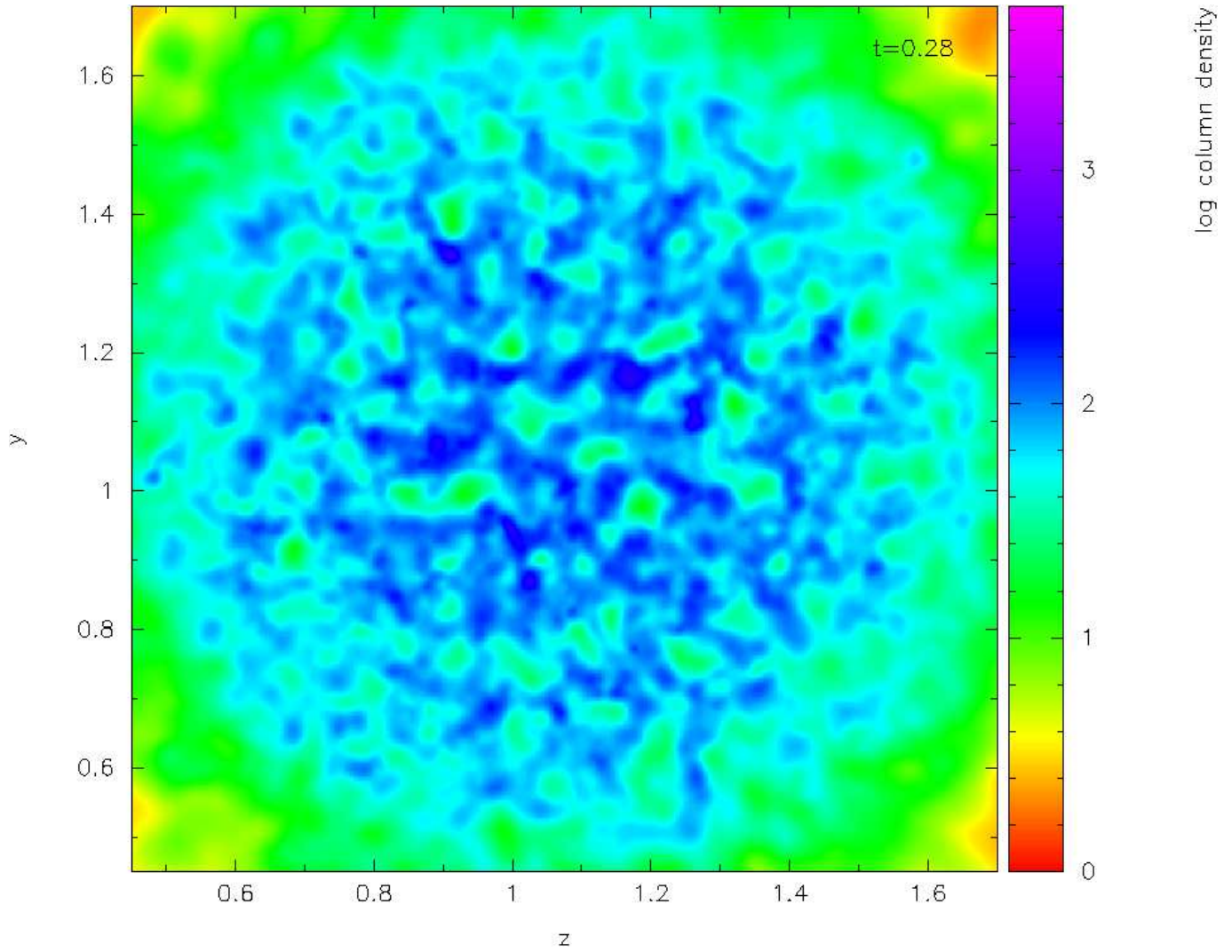


**Figure 10.** A close view of the shocked slab shortly after its formation, in model 2. It shows a network of filaments and regions of filament intersection appear denser than filaments themselves.

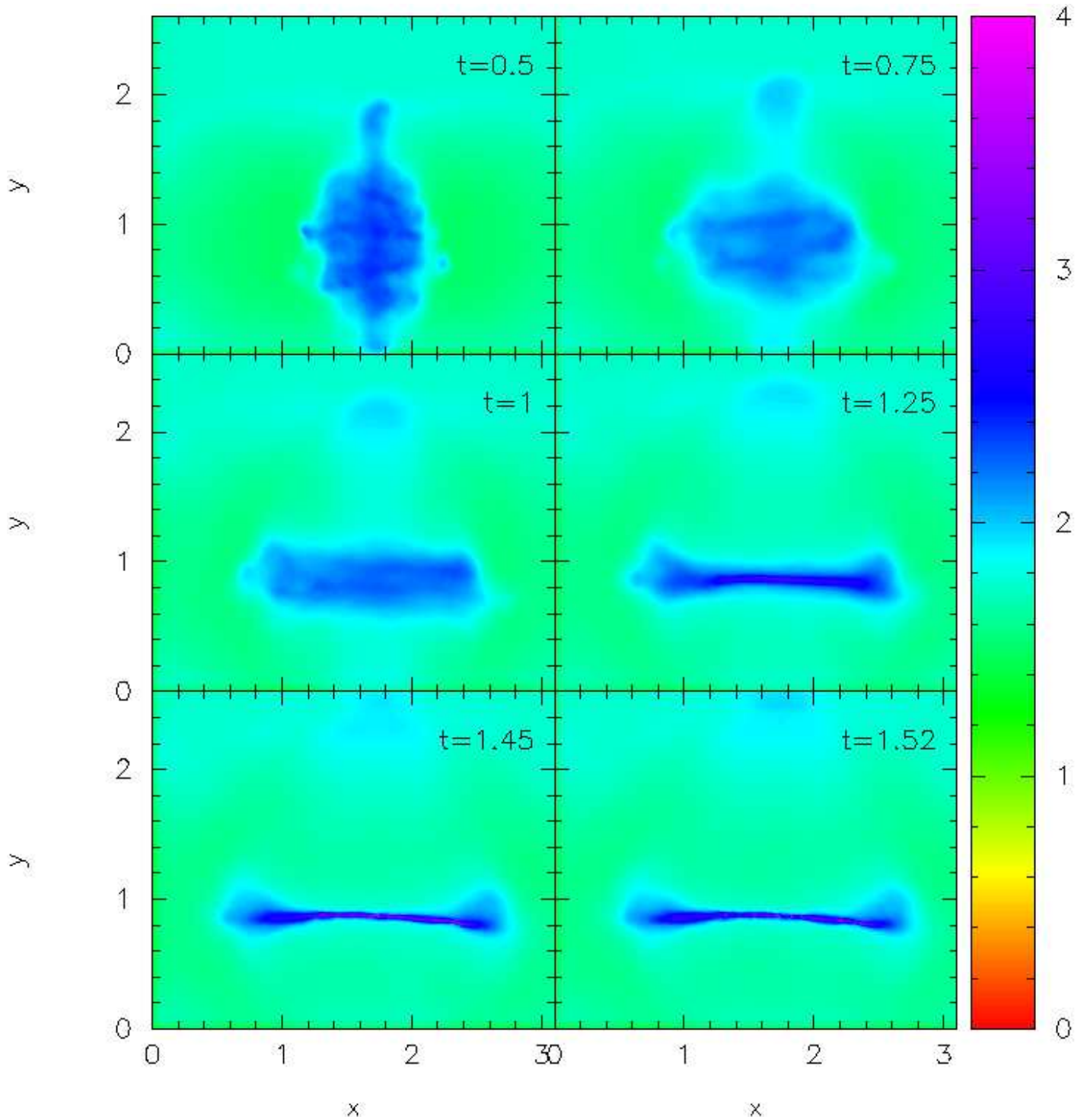


**Figure 11.** Sequence in time (Myrs) of the shocked slab collapsing to form a filament along the axis of collision ( $x$  axis), in Model 2. Material squirting out from the top and bottom ends of the shocked slab is visible in all three panels.

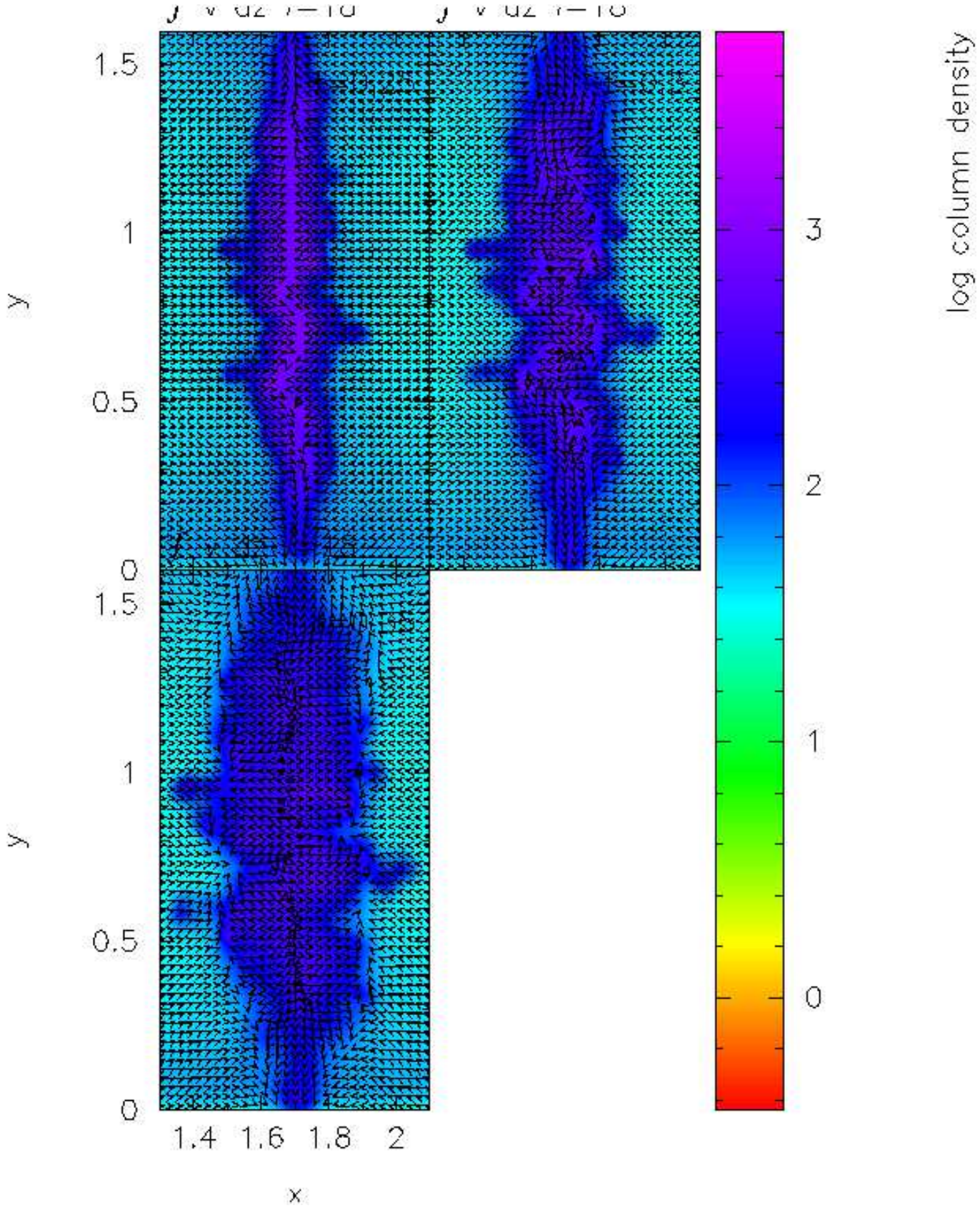


**Figure 12.** Close up of the shocked slab in model 2. The local velocity field overlaid on the column density plot shows the complex fluid flow pattern. Development of vortices, an essential feature of the KH instability, is evident in the right hand picture of the top panel. The blobs broken off from the shearing slab surface are also visible in all the three pictures.

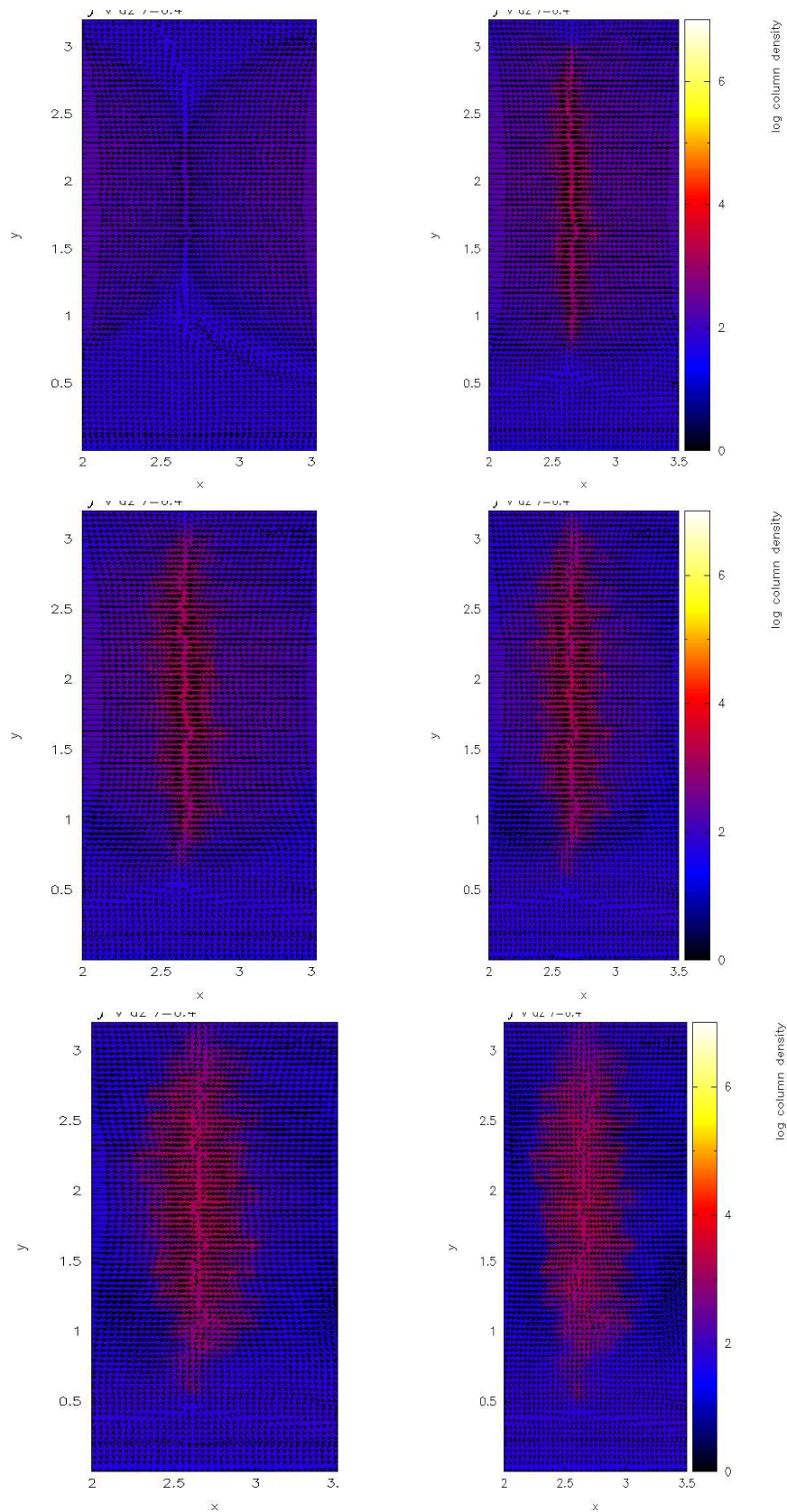


**Figure 13.** Close up of the shocked slab in model 3. The local velocity field has been overlaid on the column density plot to facilitate inferring the complex fluid flow pattern. Close inspection of the pictures reveals a few break away blobs in the vicinity of the slab surface.

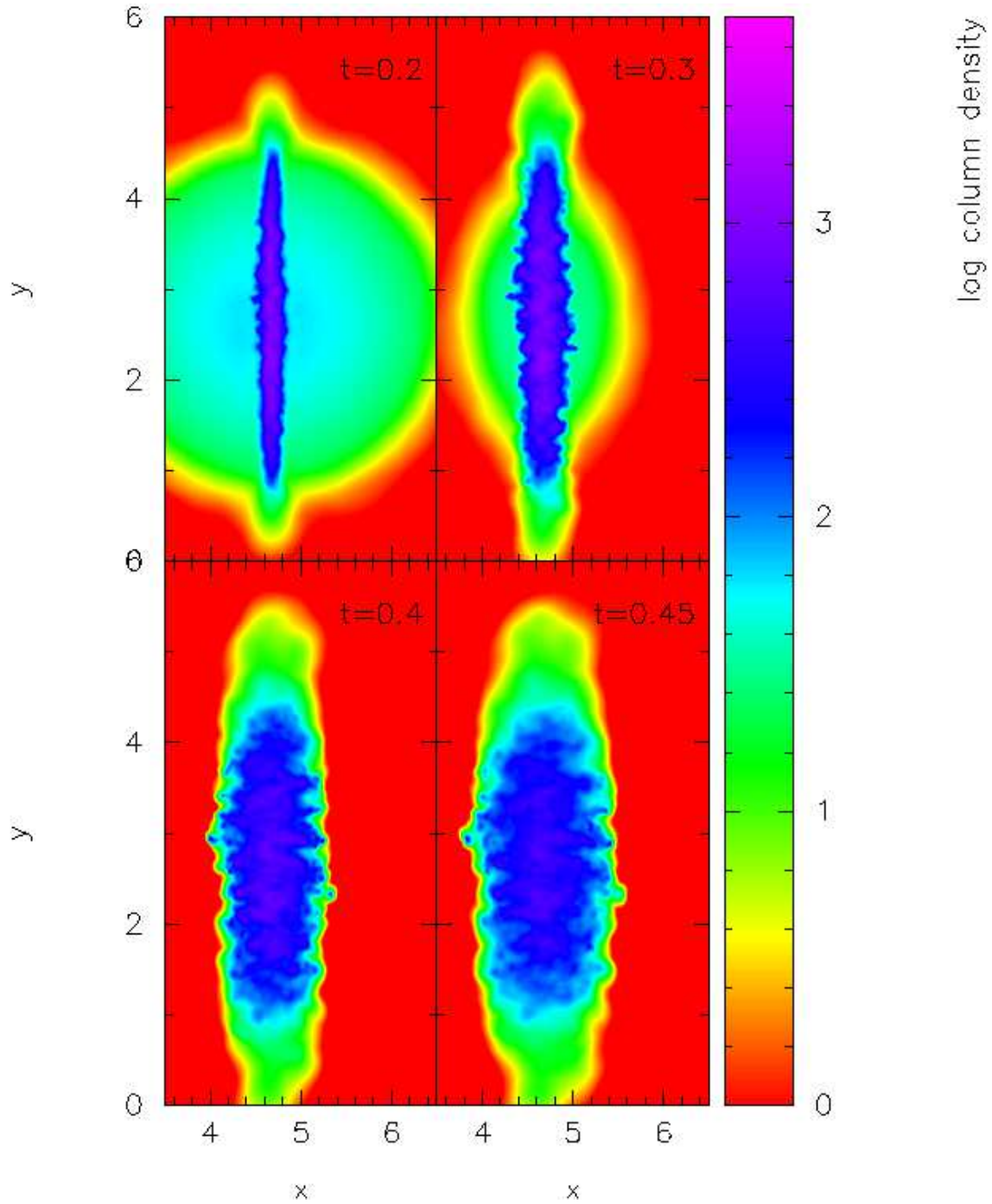


**Figure 14.** The formation of the shocked slab (model 5) and subsequent development of bending and breathing modes is visible in all the pictures of the two panels. In fact the fully grown NTSI is visible in the lower panel. Breakaway blobs near the slab surface are also visible in these pictures.

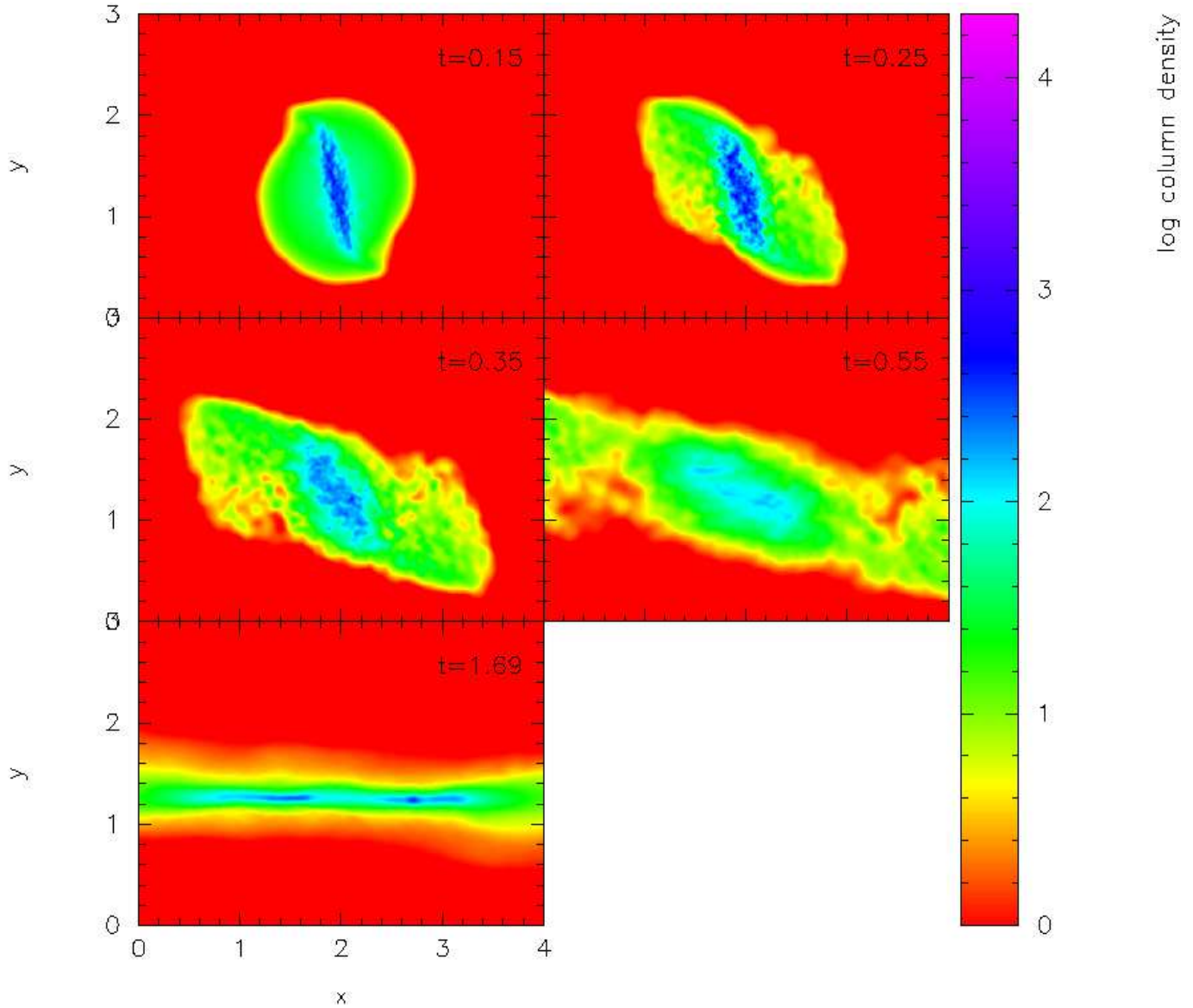


**Figure 15.** The collision of clouds in model 6. The off-centre cloud collision leads to the formation of an oblique shocked slab as can be seen in the top panel. The shocked slab then breaks into three parts and the outer two lobes of the slab move away from the central region of the slab. The slab continues to tumble about the  $z$  axis (also its angular momentum axis) and finally forms a filament parallel to the  $x$  axis.

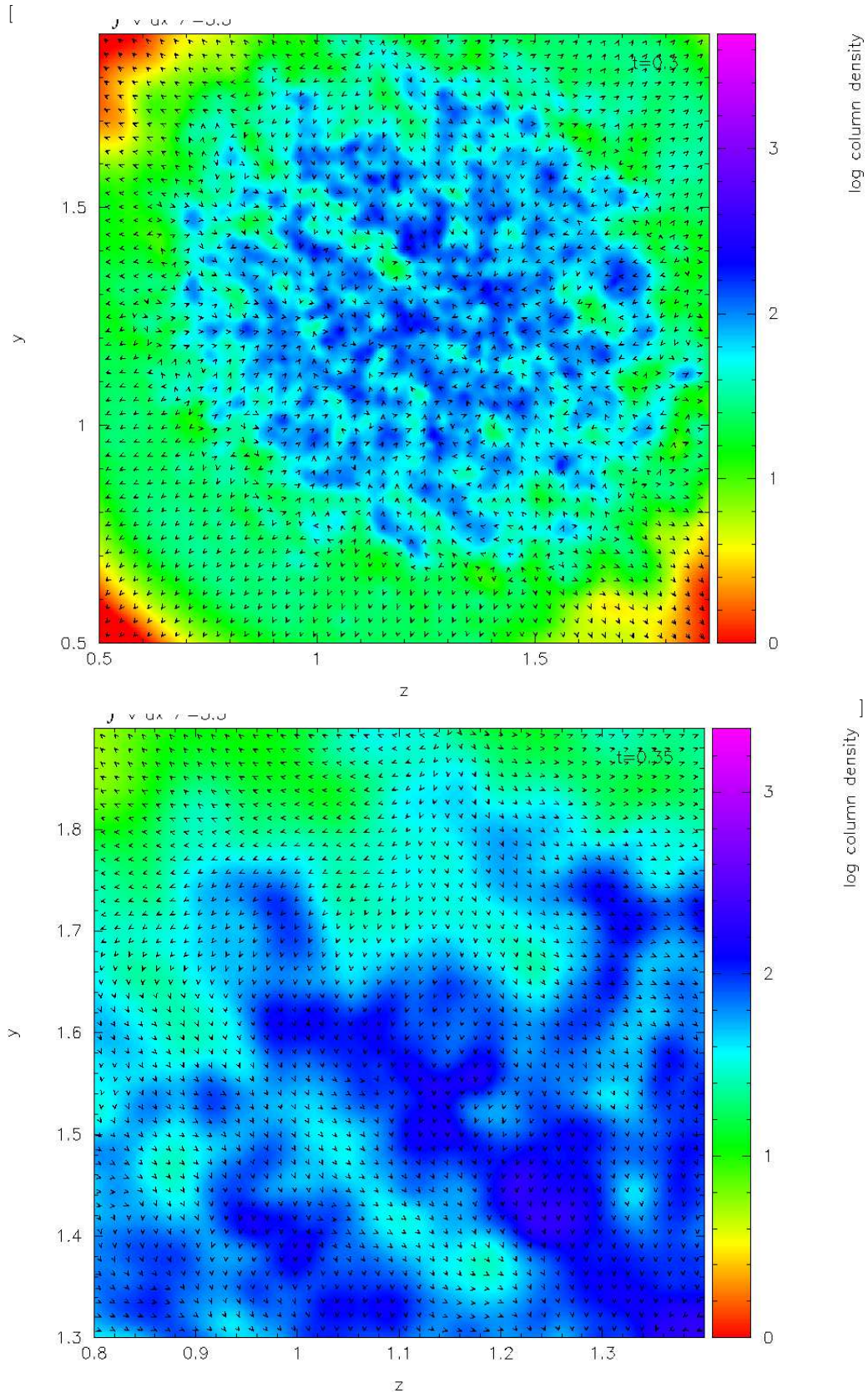


**Figure 16.** The face-on view of the oblique shocked slab formed in model 6. In the top panel, initial structure formation is clearly visible. It shows well defined filamentary regions and clumps. The velocity field overlaid on this plot shows the turbulent motion within the slab. Smaller clumps merge to form larger clumps. The picture in the lower panel shows formation of larger clumps through merger of smaller clumps.